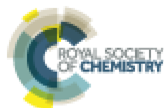

Nanoscale

Gallium, neon and helium focused ion beam milling of thin films demonstrated for polymeric materials: Study of implantation artifacts

Journal:	*Nanoscale*
Manuscript ID	NR-ART-10-2018-008224.R1
Article Type:	Paper
Date Submitted by the Author:	03-Dec-2018

Complete List of Authors:	Allen, Frances; UC Berkeley, Materials Science and Engineering; Lawrence Berkeley National Laboratory, National Center for Electron Microscopy, Molecular Foundry; UC Berkeley , California Institute for Quantitative Biosciences Velez, Nathan; UC Berkeley, Materials Science and Engineering; Lawrence Berkeley National Laboratory, National Center for Electron Microscopy, Molecular Foundry Thayer, Rachel; UC Berkeley, Integrative Biology Patel, Nipam; UC Berkeley, Integrative Biology; UC Berkeley, Molecular and Cell Biology Jones, Mary Ann; Dow Chemical Company, Core R & D Analytical Sciences Meyers, Gregory; Dow Chemical Company, Core R & D Analytical Sciences Minor , Andrew ; UC Berkeley, Materials Science and Engineering; Lawrence Berkeley National Laboratory, National Center for Electron Microscopy, Molecular Foundry

SCHOLARONE™
Manuscripts

ROYAL SOCIETY OF CHEMISTRY

Journal Name

ARTICLE TYPE

Cite this: DOI: 10.1039/xxxxxxxxxx

Gallium, neon and helium focused ion beam milling of thin films demonstrated for polymeric materials: Study of implantation artifacts†

Frances I. Allen,[*a,b,c] Nathan R. Velez,[a,b] Rachel C. Thayer,[d] Nipam H. Patel,[d,e] Mary Ann Jones,[f] Gregory F. Meyers,[f] and Andrew M. Minor[a,b]

Received Date
Accepted Date

DOI: 10.1039/xxxxxxxxxx

www.rsc.org/journalname

Focused ion beam milling of ∼200 nm polymer thin films is investigated using a multibeam ion microscope equipped with a gallium liquid metal ion source and a helium/neon gas field-ionization source. The quality of gallium, neon, and helium ion milled edges in terms of ion implantation artifacts is analyzed using a combination of helium ion microscopy, transmission electron microscopy and light microscopy. Results for a synthetic polymer thin film, in the form of cryo-ultramicrotomed sections from a co-extruded polymer multilayer, and a biological polymer thin film, in the form of the base layer of a butterfly wing scale, are presented. While gallium and neon ion milling result in the implantation of ions up to tens of nanometers from the milled edge and local thinning near the edge, helium ion milling produces much sharper edges with dramatically reduced implantation. These effects can be understood in terms of the minimal lateral scatter and larger stopping distance of helium compared with the heavier ions, whereby due to the thin film geometry, most of the incident helium ions will pass straight through the material. The basic result demonstrated here for polymer thin films is also expected for thin films of hard materials such as metals and ceramics.

1 Introduction

Focused ion beam (FIB) milling is a well-established technique in materials science used for machining on the micron down to the nanometer scale. Applications include site-specific cross-sectional analysis, circuit edit and nanofabrication[1–3]. The conventional FIB microscope uses a gallium-based liquid metal ion source (LMIS) to deliver a focused gallium ion beam onto the sample to remove material in the range of tens of cubic microns, typically using picoamp to nanoamp beam currents. More recently, plasma-based FIB microscopes delivering high current beams (up to μA) of heavier ion species (e.g. Xe) have been introduced, and the atomically sharp gas field-ionization source (GFIS) delivers low current beams (down to 0.1 pA) of lighter ion species (He, Ne). While the plasma FIB is well-suited for large-volume milling of up to hundreds of cubic microns[4], the GFIS-based microscope is optimized for fabricating much smaller features such as nanogaps, nanopores, and nanoribbons[5–8].

FIB milling has been applied most widely to metals and ceramics, yet demand for FIB processing of soft materials such as polymers is increasing. The low electrical and thermal conductivities characteristic of soft materials, however, typically mean that different strategies must be adopted. Local charging of electrically insulating specimens under FIB illumination results in the local buildup of an electrostatic field causing image distortions and potentially a physical distortion of the material itself[9]. Furthermore, ion beam induced local heating of polymers can result in thermal degradation reactions involving the rearrangement and breaking of chemical bonds, as has been observed spectroscopically[10–12]. Warping of polymer thin films due to thermal softening[13] and changes in thermomechanical behavior[10] have also been reported. A straightforward method used to alleviate charging effects, and also to some extent heating effects, is to add a conductive coating to the sample in the form of a thin metal layer to act as a charge/heat sink[11]. In fact, the application of a conductive polymer coating for this purpose in place of a metal layer has also been demonstrated[14]. An alternative method used to combat charging is to implement low-energy electrons for charge neutralization[15]. Additional strategies to mitigate thermal effects include the use of a cryogenic stage to cool the specimen and

[a] Department of Materials Science and Engineering, UC Berkeley, Berkeley, CA, USA. E-mail: francesallen@berkeley.edu
[b] National Center for Electron Microscopy, Molecular Foundry, LBNL, Berkeley, CA, USA.
[c] California Institute for Quantitative Biosciences, UC Berkeley, Berkeley, CA, USA.
[d] Department of Integrative Biology, UC Berkeley, Berkeley, CA, USA.
[e] Department of Molecular and Cell Biology, UC Berkeley, Berkeley, CA, USA.
[f] Core R&D - Analytical Sciences, The Dow Chemical Company, Midland, MI, USA.

† Electronic Supplementary Information (ESI) available: See DOI: 10.1039/b000000x/

thereby limit the local temperature rise induced by the focused beam and/or to implement low milling currents (≤100 pA) to reduce the heat load on the specimen[10,13,16].

Artifacts also arise due to the implantation of ions into the specimen[1]. This effect has been well-studied for gallium FIB, in particular with respect to FIB preparation of electron transparent lamella-type samples for Transmission Electron Microscopy (TEM), where even under glancing incidence conditions a proportion of gallium ions will always be implanted[17]. The thickness of this damage layer can be reduced by reducing the beam energy (and hence the ion stopping range) in the final thinning steps[17,18]. However, the lower the beam energy the broader the beam, thereby reducing the spatial resolution, which for applications requiring a higher precision of milling is not a viable option.

In the following we use a multibeam ion microscope equipped with a gallium LMIS column and a helium/neon GFIS column to investigate gallium, neon and helium FIB milling of polymer thin films. Low milling currents are used throughout in order to minimize heating effects and thus enable the study to focus on implantation artifacts and milling fidelity for each of the three beams. The first polymer sample is a synthetic polymer in the form of a co-extruded multilayer consisting of polypropylene and the ethylene-octene-based elastomer ENGAGE™ Polyolefin Elastomer (POE) (an impact modifier). Thin film cross sections through the multilayer are prepared by cryo-ultramicrotomy and FIB-milled regions are then studied at the nanoscale by TEM, scanning TEM (STEM), and STEM-based elemental mapping by X-ray energy dispersive spectrometry (XEDS). The second polymer sample is the biological polymer chitin (a polysaccharide), in the form of a butterfly wing scale. Light microscopy (LM) plan view imaging and helium ion microscopy (HIM) tilt view imaging of edges milled into the base membrane of the scale (the so-called lamina) are used to assess the quality of the FIB mills obtained using each of the three beams.

2 Experimental

2.1 FIB milling of polymer multilayer

Thin sections (∼200 nm) from a polypropylene-ENGAGE™ POE multilayer sheet were prepared by cryo-ultramicrotomy and placed onto carbon-stabilized lacey formvar TEM grids (Ted Pella). The FIB milling was performed using a Zeiss ORION NanoFab multibeam ion microscope (the nominal probe sizes of the gallium, neon and helium ion beams are 3, 1.9 and 0.5 nm, respectively, as determined using the common rise-distance method, imaging across a sharp edge). Figure 1 shows a tilt-view HIM image of a thin section of the polymer multilayer on the TEM support after a series of slots had been milled into the film. The milled regions are the bright rectangles aligned with their long axes perpendicular to the direction of the microlayers of the film. The inset shows a higher magnification high-angle annular dark field (HAADF) STEM view of the microlayers. A conductive coating was not applied to these samples since significant charging effects under FIB illumination were not observed.

™ Trademark of the Dow Chemical Company

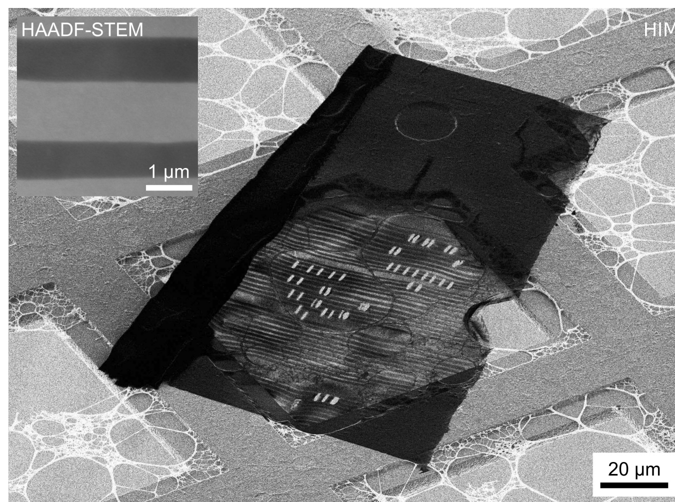

Fig. 1 HIM of a cryo-ultramicrotomed section of the polypropylene-ENGAGE™ POE multilayer on a lacey formvar TEM support (stage tilt 54°) showing the alternating microlayers and a series of FIB-milled slots. A higher magnification dark-field STEM view of the microlayers is shown inset.

In order to facilitate direct comparison of the FIB milling results for the three ion species, experiments using the same beam energy (25 keV) for each ion beam were performed. Low milling currents (≪100 pA) were implemented in order mitigate local heating effects upon FIB milling of the polymer thin films[13]. The current of the gallium ion beam was set to 10 pA using the appropriate beam-limiting aperture, and the neon and helium ion mills were performed using beam currents of 10 pA (10 μm aperture, 2×10^{-6} Torr Ne, spot 4) and 18 pA (40 μm aperture, 2×10^{-6} Torr He, spot 4), respectively. The slightly higher helium ion beam current was selected for practical reasons due to the light ion's inherently low sputter rate.

Regions for milling were located by HIM under low-dose conditions and rectangular mills were performed (under normal incidence) using the NanoPatterning and Visualization Engine (NPVE) pattern generator from Fibics Inc. The dimensions of the rectangles milled with gallium and neon were set to $0.5\times4\,\mu m^2$ and $0.25\times4\,\mu m^2$, respectively. In the case of the helium mills, smaller rectangles ($0.2\times3\,\mu m^2$) were positioned to overlap with the edge of a gallium mill in order to reduce the total mill time and allow direct comparison of edges milled with gallium versus helium. Endpoint detection in NPVE was used to determine the dose per area required to complete the various mills, where a drop in secondary electron yield signaled the dose at which total removal of material in the patterned region was achieved. The milling doses subsequently implemented were 0.045, 2 and 15 nC/μm^2 for the gallium, neon, and helium FIB mills, respectively. The scan parameters for the mills were set to the default NPVE values: dwell time 1 μs, pixel spacings 0.25 nm (He and Ne), and 3 nm (Ga).

(S)TEM imaging and analysis of the milled polymer was carried out using a Zeiss Libra 200MC microscope operated at 200 kV and an FEI TitanX microscope operated at 80 kV. Elemental mapping by STEM-XEDS was performed using a Bruker windowless

This journal is © The Royal Society of Chemistry [year]

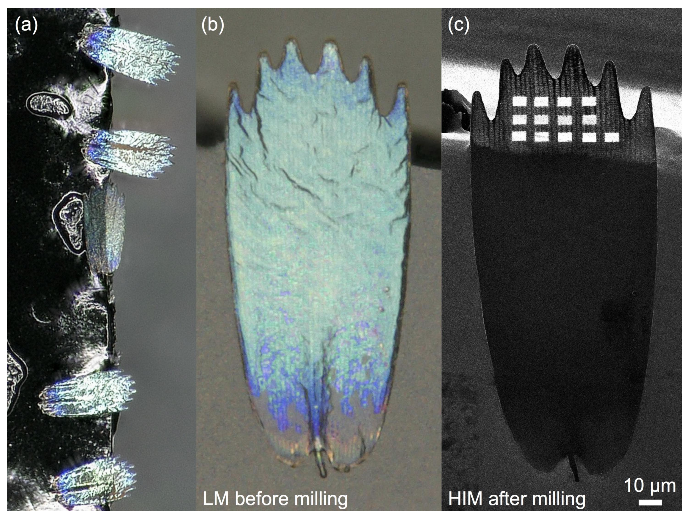

Fig. 2 (a) LM of edge-mounted butterfly wing scales, (b) LM of a single edge-mounted scale, (c) HIM of the single scale after FIB milling.

quadrature x-ray detector with solid angle of 0.7 sr on the TitanX microscope and using Bruker Esprit software. Simulations of the ion distributions in thin-film targets were performed using Stopping and Range of Ions in Matter (SRIM) software [19], selecting the appropriate beam energies and polypropylene as the target material.

2.2 FIB milling of chitin

The butterfly wing scale specimens (i.e. the biological polymer, chitin) were extracted from the Buckeye butterfly *Junonia coenia* under a Zeiss Stemi SV 11 dissection microscope and mounted onto conductive carbon tape. Blue scales were selected for this study, with a lamina thickness of ∼200 nm. The scales were mounted such that free-standing regions could be used for the milling runs in order to avoid substrate effects such as swelling (especially important in the case of He-FIB). This was achieved in one of two ways, either using a low-profile stepped (90°) FIB pin stub whereby the scales were mounted on the horizontal step edge onto carbon tape such that they protruded over the edge by half their length or less, or, using a standard flat Scanning Electron Microscopy (SEM) stub and bridge-mounting scales over a narrow gap scribed into the carbon tape using a razor blade. Figure 2(a) shows an LM view of several scales mounted using the step edge method, 2(b) shows a higher magnification LM view of a single edge-mounted scale, and 2(c) shows an HIM view of a set of rectangles that were FIB-milled into the free-standing edge of the scale.

Charge-induced bending of the specimens was observed when FIB milling and imaging uncoated scales, hence a conductive coating of ∼0.8 nm gold-palladium was added using a glow-discharge sputter coater for the milling experiments. Optical images of scales before and after coating confirmed that only a slight dulling of the scale's blue color upon coating resulted (see Supplementary Figure S1).

Scales with the lamina side facing upwards were located by HIM under low-dose conditions (low current, short dwell time, small scan size, relatively large field-of-view snapshot imaging), using the LM overview images as a guide. Rectangular regions, typically $4\times6\,\mu m^2$, were milled using the gallium ion beam at 30 keV using a beam current of 100 pA. Neon and helium ion milling over smaller areas at the edges of gallium-milled rectangles and/or in isolated regions was performed at 25 keV using currents of 10 and 19 pA, respectively, using the same beam settings as for the synthetic polymer. Typical milling doses implemented were 0.4–1, 1–3 and 10–12 $nC/\mu m^2$ for gallium, neon, and helium, respectively. The scan parameters (dwell times, pixel spacings) for all three beams were set to the same values implemented previously. Care was taken throughout to minimize exposure of the scales to the ion beams between mills, i.e. all focusing was performed on regions at the base of the scale (socket end), far from the region of interest used for patterning. The acquisition of snapshot images between mills was also kept to a minimum. We note that while the gallium FIB current was higher in this experiment (due to the larger volume of material to be removed), it was still low enough that thermal effects such as local warping around milled regions were not observed.

Post milling, LM imaging of the scales was performed using a Keyence VHX-5000 digital microscope using the 500-5000x lens, after which samples were returned to the ion microscope for higher resolution HIM imaging of the FIB-milled edges under a stage tilt of 54°.

3 Results and discussion

3.1 FIB milling of polymer multilayer

Summaries of the experimental results for the synthetic polymer thin film for gallium, neon and helium FIB milling are shown in Figures 3(a), (b), and (c), respectively. The schematics show the dimensions of the mills implemented for each ion species, alongside the HAADF-STEM images and corresponding gallium and neon elemental maps obtained by STEM-XEDS. The light and dark bands in the STEM images correspond to the alternating polypropylene and ENGAGE™ POE layers, respectively, of the sectioned multilayer.

In the gallium FIB result of Figure 3(a), a bright rim is observed in the HAADF-STEM image along the perimeter of the milled region. The adjacent elemental map reveals that this bright rim (indicative of a higher atomic number species than carbon) corresponds to implanted gallium. In the neon FIB case seen in Figure 3(b), the milled edges are more uneven indicating that the mill with the lighter neon ions was less efficient (even though a higher ion dose was implemented than for the gallium mill, evidently in this case it should have been slightly greater still in order to achieve a sharper edge). The elemental map for neon shows that similarly to the gallium case, neon is implanted at the edge of the milled region, consistent with previous studies of neon milling of aluminum and silicon [20]. In the helium FIB result of Figure 3(c), we see that the high-dose helium ion mill was able to clean up an edge pre-milled with gallium, leaving a straight edge free from implanted gallium ions. We note that helium mapping by STEM-XEDS is not possible, since for this element a characteristic X-ray does not exist.

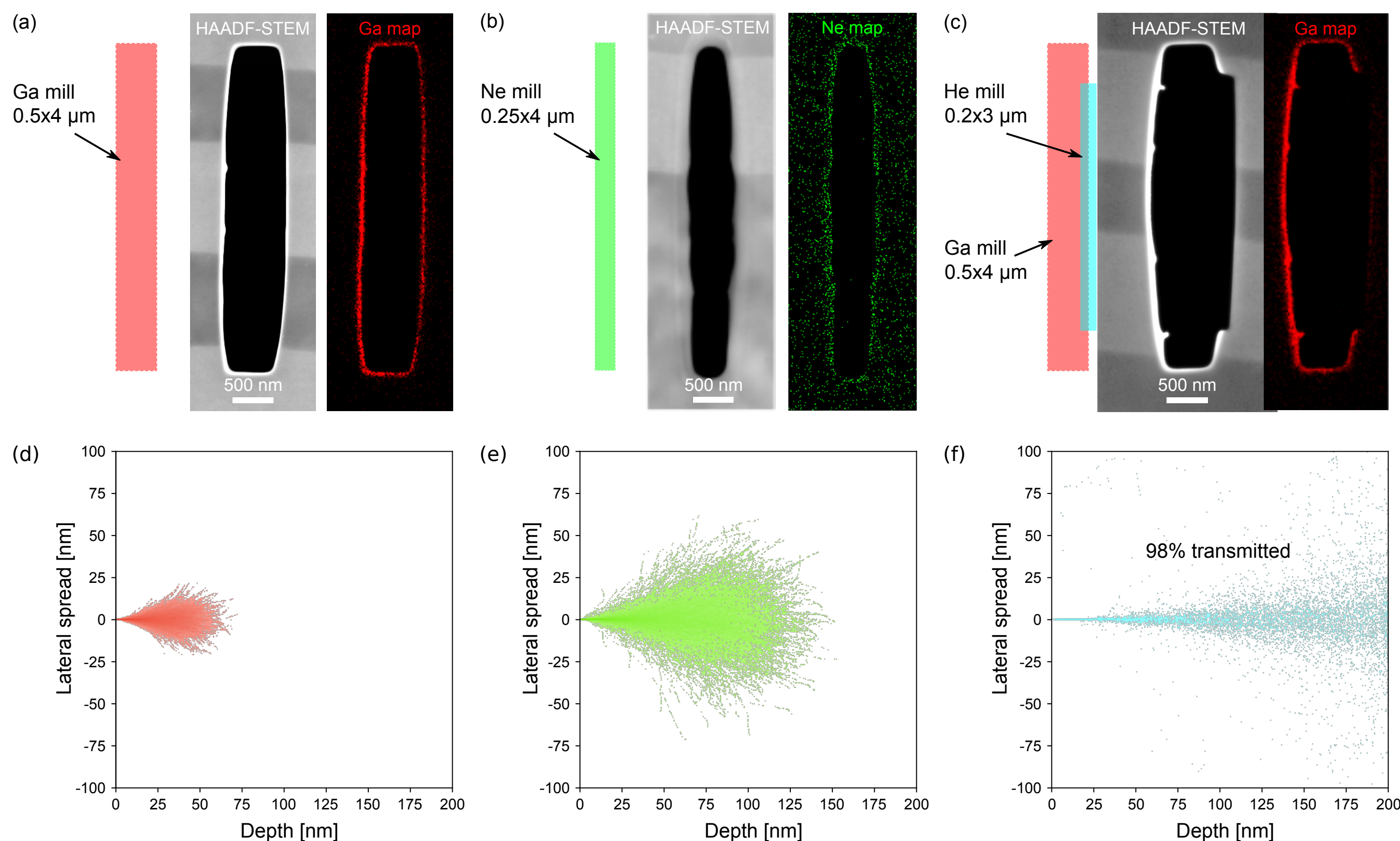

Fig. 3 Experimental results for FIB milling of the synthetic polymer multilayer thin film using (a) 25 keV Ga^+ (10 pA), (b) 25 keV Ne^+ (10 pA), and (c) 25 keV He^+ ions (20 pA). The color boxes show the dimensions of the milling patterns used for each ion species: Ga^+ (red), Ne^+(green), He^+ (cyan). (Note the He-mill test is confined to a 'clean-up' of one side of a Ga-milled rectangle). HAADF-STEM images and the respective STEM-XEDS Ga and Ne elemental maps are shown. SRIM simulations for the stopping ranges of 25 keV Ga^+, Ne^+, and He^+ in 200 nm polypropylene under normal incidence are shown in (d), (e), and (f), respectively, plotted using a logarithmic color scale.

The Monte Carlo SRIM simulation results for the stopping ranges of the three ion species (incident energy 25 keV) in 200 nm polypropylene targets are shown in Figures 3(d–f). A striking difference becomes apparent, in that all of the gallium and neon ions are implanted within the film thickness in a tear-drop shaped volume, whereas the helium ions scatter much less and in fact 98 % are transmitted through the membrane. While the membrane is of course sputtered and hence becomes thinner as a result of the ion bombardment (SRIM does not account for these dynamic effects), the simulations predict significant implantation of both gallium and neon ions into the border of a milled pattern, as indeed was observed in the experiment. We note that the lateral spread determined by the gallium SRIM simulation in Figure 3(d) is approximately $\pm$20 nm, whereas in the corresponding experimental STEM-XEDS elemental map (Figure 3(a)), the thickness of the implanted gallium region is around twice that value, at $\sim$40 nm. This broadening is likely explained by the actual current density profile of the gallium ion beam, which is Gaussian-like and can have significant beam tails[21], in contrast to the SRIM simulations, where a point-like beam is assumed. In the neon case (Figure 3(e)), SRIM predicts a larger interaction volume with a lateral spread of up to $\pm$70 nm. While the signal-to-noise ratio in the neon elemental map is too low to enable an absolute comparison of the theoretical and experimental lateral spreads, the measured neon distribution does appear to be more diffuse than in the gallium case, which also explains the lack of a contrast change in the HAADF-STEM image. In terms of the actual current density profile, a sharper Gaussian component for the central beam and weaker beam tails are expected for the GFIS-generated beams[22]. As mentioned, STEM-XEDS does not allow elemental mapping of helium. However, referring to the SRIM result for helium shown in Figure 3(f) and considering that the membrane becomes progressively thinner as the milling proceeds, we predict that less than 1 % of the total incident helium ions will be implanted at the perimeter of the helium-milled edge. It is well known that upon irradiation at high enough doses, implanted helium (and neon) can result in bubble/blister formation in the target material[23,24], yet as discussed, negligible implantation of helium is expected for our thin film geometry. Moreover, higher magnification TEM imaging of the helium-milled edges did not detect any evidence of nanobubble formation (see Supplementary Figure S2).

3.2 FIB milling of chitin

Results from gallium FIB milling of the biological polymer chitin are presented in Figure 4. The LM image of Figure 4(a) shows six milled rectangles, the pattern dimensions of which are shown drawn to scale in the schematic inset. A higher magnification tilt-

 This journal is © The Royal Society of Chemistry [year]

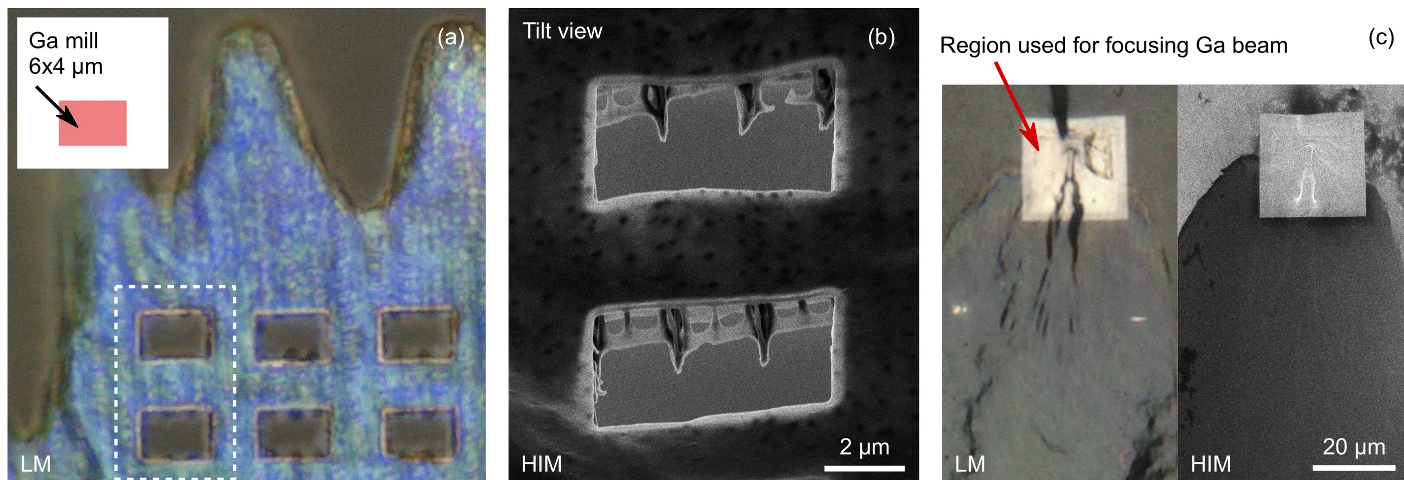

Fig. 4 Gallium FIB milling of chitin (30 keV, 100 pA). (a) LM of rectangles milled and schematic showing dimensions of mills. (b) HIM tilt view (stage tilt 54 °) of the two rectangles outlined in (a). (c) LM and HIM of a square region at the base of the butterfly wing scale that was exposed to gallium during beam focusing.

view HIM image of two of the rectangles, outlined by the dashed white line, is shown in Figure 4(b). The structures beneath the thin film/lamina, which are revealed by the FIB mills and subsequent HIM imaging under tilt, are the rib and cross-rib structures also characteristic of butterfly wing scales (and which are also composed of chitin). Interestingly, the rims of the milled rectangles have an orange/gold color in the LM image and show bright contrast in the HIM image. As has been shown by the elemental mapping and simulation results of Figure 3, lateral scatter of gallium ions up to several tens of nanometers occurs. Consequently, sputtering resulting in thinning beyond the perimeter of a given milled region is expected. The dependence of optical reflectance spectra on lamina thickness is in fact one of several phenomena known to determine the color of individual butterfly wing scales[25], hence local thinning of the lamina near the milled edges could be responsible for the color change observed in the LM images. (Direct evidence for the local thinning is discussed below). Figure 4(c) shows an optical image (left) and HIM image (right) of the socket-end of the butterfly wing scale, which was used as a sacrificial region for focusing of the gallium beam. In the LM image, the focusing region is clearly visible as a gold square, and in the HIM image as a square of brighter contrast. In this example, the membrane is supported by a bulk substrate, which will alter the reflectance behavior of the thin film and yet both it and the surrounding carbon support appear to have turned the same gold color, which is close to the color of the rims observed in Figure 4(a). Thus possibly specular reflection from the implanted gallium also contributes to the color change observed, and/or a thin film reflectance effect from the implanted gallium layer itself may be at play. The bright contrast of the exposed region in the HIM image is likely due to the surface conductivity imparted by the implanted gallium, which electrically grounds the exposed region to the carbon support. Material contrast from the gallium may also be a contributing factor.

The neon FIB milling results for the chitin specimen are shown in Figure 5. Here, the neon ion beam was first used to mill a rectangle into one side of a gallium-milled region, as shown in Figure 5(a). Next, much smaller rectangles were milled only using neon (i.e. no pre-mill with gallium), as shown in Figure 5(b). The schematics in the figures showing the dimensions of the milled regions are scaled to the LM images. We observe that the neon-milled regions again exhibit golden rims in the LM images and rims with brighter contrast in the HIM views, even in the complete absence of gallium. Moreover, in the higher magnification HIM tilt view of Figure 5(b), a marked thinning of the membrane around the mills is observed (see white arrows highlighting step-shaped edges), which lends support to the hypothesis of color change due to a change in spectral reflectance from the thinned lamina.

Finally, the LM and HIM results for helium FIB milling of chitin, together with a comparison of higher magnification HIM tilt views of the gallium, neon, and helium milled edges, are shown in Figure 6. The helium beam was used to mill one side of a gallium-milled rectangle, as shown in Figure 6(a) (again, the schematic is scaled to the LM image). We note that in this experiment, the gallium FIB milling dose was at the lower end of the range implemented, which explains why here, the ribs and cross-ribs beneath the lamina were not completely removed. In the LM image, a gold rim extending around the border of the gallium-milled region is again observed, but in the area of the helium mill, this gold rim is interrupted (region highlighted by the dashed white box). This indicates that the helium mill not only removed the gallium-milled rim (as was observed for helium FIB milling of the synthetic polymer in Figure 3(c)), but also that the helium-milled edge is sharper with much less thinning near the edge than its gallium, and neon, counterparts.

The higher magnification HIM tilt views in Figure 6(b) show in more detail the stepped edges (step widths of a few tens of nanometers, due to local thinning) obtained for the gallium and neon FIB mills versus the much sharper edge obtained for the helium FIB mill. As discussed previously, the gallium and neon ions scatter laterally to a much greater extent than the light he-

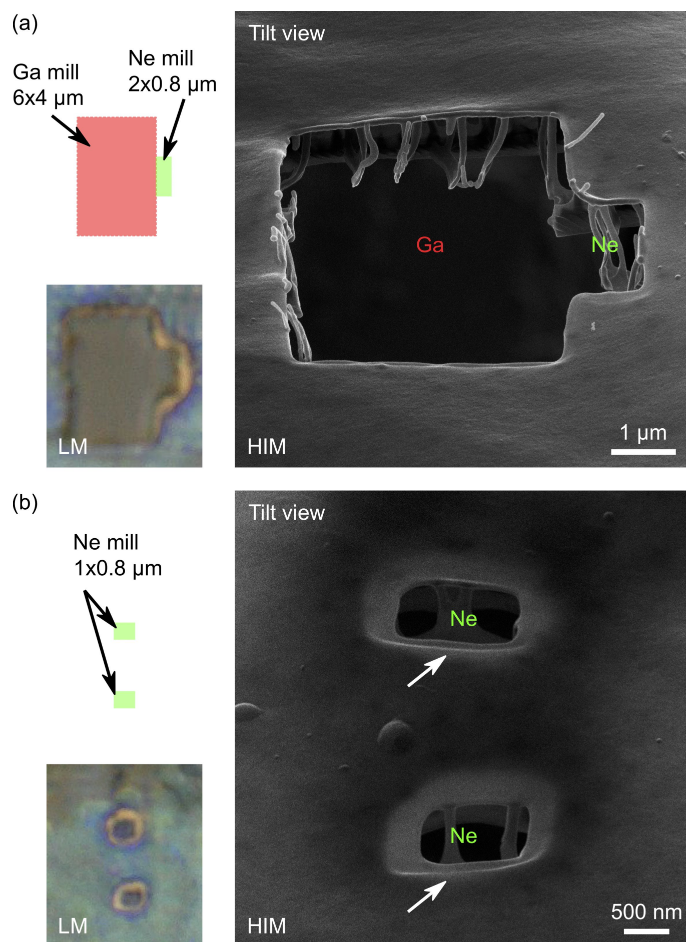

Fig. 5 Neon FIB milling of chitin (25 keV, 10 pA). (a) Neon mill at the edge of gallium-milled rectangle, showing schematic of box dimensions, LM and HIM tilt views. (b) Neon mills without gallium pre-mill, showing schematic of box dimensions, LM and HIM tilt views.

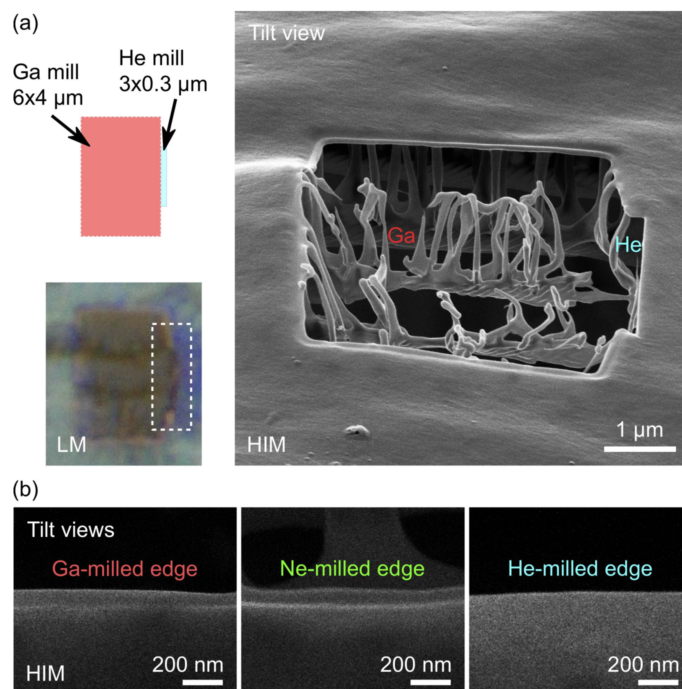

Fig. 6 Helium FIB milling of chitin (25 keV, 19 pA) and summary of results for edges milled with gallium, neon and helium. (a) Helium mill at edge of gallium-milled rectangle. Schematic of box dimensions, LM view and HIM tilt view are shown. (Here, the gallium FIB dose is lower than in previous mills, explaining why rib structure beneath the lamina not completely removed). (b) Higher magnification HIM tilt-view images of gallium, neon and helium FIB-milled edges.

lium ions, hence as well as sputtering material inside the defined region to be milled, the gallium and neon ions sputter a border region outside the perimeter as well, albeit at a slower rate since the total dose received by that region is lower. This leads to a step edge outside the milled region. Comparing the dimensions of the milling patterns implemented to the resulting LM and HIM images confirms that the step edges are formed outside the patterned regions. In contrast, most of the helium ions transmit the membrane with minimal lateral scatter, resulting in much sharper edges.

4 Conclusions

Gallium and neon FIB milling of the polymer thin films resulted in the implantation of ions forming a border a few tens of nanometers in thickness around the milled edges, with the associated thinning resulting in a step edge, whereas helium FIB milling enabled much sharper cuts with negligible implantation. These results demonstrate the advantage of FIB milling a thin-film geometry (polymer or otherwise) with a light ion that undergoes minimal lateral scatter and has a stopping distance in the film greater than the film thickness, i.e. the majority of the ions will not be implanted and the milled edge will be sharp and free from contamination. Since helium FIB milling is much slower than gallium FIB milling (due to the lighter mass of helium and lower currents attainable from GFIS technology), helium FIB is most favorably employed for precise milling of small volumes either in a one-step process, or in a clean-up step following gallium FIB-milling of a larger volume. However, for thicker samples, possible subsurface damage from the implantation of helium into the material, which at high dose can result in the formation of helium bubbles and blistering[23,24], must be considered.

Acknowledgements

F.I.A., N.R.V., M.A.J., G.F.M. and A.M.M. acknowledge support from the Dow University Partnership Initiative Program. R.C.T. and N.H.P. acknowledge support from NSF Department of Environmental Biology Grant 1601815 and the NSF Graduate Research Fellowship Program. Work at the Molecular Foundry at Lawrence Berkeley National Laboratory was supported by the U.S. Department of Energy under Contract # DE-AC02-05CH11231. We thank John Notte and David Ferranti of Carl Zeiss Microscopy for helpful discussions.

References

1 C. A. Volkert and A. M. Minor, *MRS Bulletin*, 2007, **32**, 389–399.
2 M. W. Phaneuf, *Micron*, 1999, **30**, 277–288.
3 A. Tseng, *Small*, 2005, **1**, 924–939.

This journal is © The Royal Society of Chemistry [year]

4 T. L. Burnett, R. Kelley, B. Winiarski, L. Contreras, M. Daly, A. Gholinia, M. G. Burke and P. J. Withers, *Ultramicroscopy*, 2016, **161**, 119–129.

5 A. N. Abbas, G. Liu, B. Liu, L. Zhang, H. Liu, D. Ohlberg, W. Wu and C. Zhou, *ACS Nano*, 2014, **8**, 1538–1546.

6 J. Yang, D. C. Ferranti, L. A. Stern, C. A. Sanford, J. Huang, Z. Ren, L.-C. Qin and A. R. Hall, *Nanotechnology*, 2011, **22**, 285310.

7 A. Belianinov, M. J. Burch, S. Kim, S. Tan, G. Hlawacek and O. S. Ovchinnikova, *MRS Bulletin*, 2017, **42**, 660–666.

8 M. G. Stanford, B. B. Lewis, K. Mahady, J. D. Fowlkes and P. D. Rack, *J. Vac. Sci. Technol. B*, 2017, **35**, 030802.

9 D. C. Tanugi and N. Yao, *J. Appl. Phys.*, 2008, **104**, 063504.

10 C. C. Lee, G. Proust, G. Alic, G. M. Spinks and J. M. Cairney, *Journal of Microscopy*, 2012, **248**, 129–139.

11 N. D. Bassim, B. T. de Gregorio, A. L. D. Kilcoyne, K. Scott, T. Chou, S. Wirick, G. Cody and R. M. Stroud, *Journal of Microscopy*, 2012, **245**, 288–301.

12 A. Orthacker, R. Schmied, B. Chernev, J. E. Fröch, R. Winkler, J. Hobisch, G. Trimmel and H. Plank, *Phys. Chem. Chem. Phys.*, 2014, **16**, 1658–1666.

13 S. Kim, M. J. Park, N. P. Balsara, G. Liu and A. M. Minor, *Ultramicroscopy*, 2011, **111**, 191–199.

14 M. S. Alias, H.-Y. Liao, T. K. Ng and B. S. Ooi, *J. Vac. Sci. Technol. B*, 2015, **33**, 06F701.

15 R. H. Livengood, Y. Greenzweig, T. Liang and M. Grumski, *J. Vac. Sci. Technol. B*, 2007, **25**, 2547–2552.

16 M. Marko, C. Hsieh, W. Moberlychan, C. A. Mannella and J. Frank, *Journal of Microscopy*, 2007, **222**, 42–47.

17 J. Mayer, L. A. Gianuzzi, T. Kamino and J. Michael, *MRS Bulletin*, 2007, **32**, 400–407.

18 S. Bals, W. Terry, R. Geurts, Z. Yang and D. Schryvers, *Microsc. Microanal.*, 2007, **13**, 80–86.

19 J. F. Ziegler, M. D. Ziegler and J. P. Biersack, *Nuclear Instruments and Methods in Physics Research B*, 2010, **268**, 1818–1823.

20 T. C. Pekin, F. I. Allen and A. M. Minor, *Journal of Microscopy*, 2016, **264**, 59–63.

21 Y. Greenzweig, Y. Drezner, S. Tan, R. H. Livengood and A. Raveh, *Microelectronic Engineering*, 2016, **155**, 19–24.

22 K. T. Mahady, S. Tan, Y. Greenzweig, A. Raveh and P. D. Rack, *Nanotechnology*, 2018, **29**, 495301.

23 R. Livengood, S. Tan, Y. Greenzweig, J. Notte and S. McVey, *J. Vac. Sci. Technol. B*, 2009, **27**, 3244–3249.

24 S. Tan, R. Livengood, D. Shima, J. Notte and S. McVey, *J. Vac. Sci. Technol. B*, 2010, **28**, C6F15–C6F21.

25 D. G. Stavenga, H. L. Leertouwer and B. D. Wilts, *J. Exp. Biol.*, 2014, **217**, 2171–2180.

This journal is © The Royal Society of Chemistry [year]

The focused helium ion beam is ideally suited to precision milling of thin films avoiding implantation artifacts